nature materials

ARTICLES

PUBLISHED ONLINE: 18 MAY 2015 | DOI: 10.1038/NMAT4288

Measuring surface dislocation nucleation in defect-scarce nanostructures

Lisa Y. Chen[1], Mo-rigen He[1], Jungho Shin[1], Gunther Richter[2] and Daniel S. Gianola[1]*

Linear defects in crystalline materials, known as dislocations, are central to the understanding of plastic deformation and mechanical strength, as well as control of performance in a variety of electronic and photonic materials. Despite nearly a century of research on dislocation structure and interactions, measurements of the energetics and kinetics of dislocation nucleation have not been possible, as synthesizing and testing pristine crystals absent of defects has been prohibitively challenging. Here, we report experiments that directly measure the surface dislocation nucleation strengths in high-quality ⟨110⟩ Pd nanowhiskers subjected to uniaxial tension. We find that, whereas nucleation strengths are weakly size- and strain-rate-dependent, a strong temperature dependence is uncovered, corroborating predictions that nucleation is assisted by thermal fluctuations. We measure atomic-scale activation volumes, which explain both the ultrahigh athermal strength as well as the temperature-dependent scatter, evident in our experiments and well captured by a thermal activation model.

The nearly century-long study of the structure and interactions of dislocations has been crucial for elucidating the properties and mechanical response of crystalline materials. Even before the invention of the transmission electron microscope (TEM), which facilitated direct observations of such defects[1], the concept of dislocations as a mechanism explaining the discrepancy between the theoretical strength in perfect crystals and the actual measured strength in real crystals had been proposed and developed[2–4]. The evidence of dislocations not only explained the ductile behaviour and work hardening abilities of metals relevant to structural applications for many centuries prior, but also informed other poorly understood phenomena in crystalline materials, such as rapid crystal growth[5], the facilitation of diffusion-less phase transformations[6], alloy corrosion[7], degradation of optoelectronic response[8], mobility enhancements in strained semiconductors[9], and solid-state amorphization in phase change devices[10].

Despite a rich understanding of the structure of dislocations pre-existing within crystals, their interactions with other defects, and even their annihilation, until recently it has been extremely challenging to address the details of the introduction—or nucleation—of dislocations in pristine crystals. In bulk crystals, the presence of pre-existing dislocations following synthesis or treatment is ubiquitous given the extreme conditions during crystal growth and relatively low energy barriers for nucleation, yet descriptions of their origin remain largely phenomenological. Nanostructured materials, on the other hand, can be synthesized with few or even zero defects, owing to the minuscule volumes of material and near-equilibrium crystal growth[11,12]. These materials, thus, operate in a regime where conventional dislocation processes are abated and must rely on nucleation to relieve large stresses and facilitate plastic deformation if brittle fracture is to be mitigated. As a large fraction of atoms in nanostructures resides at surfaces and interfaces, these materials are particularly prone to heterogeneous dislocation nucleation at ultrahigh stresses approaching the theoretical limit[12]. In these extreme settings, deformation mechanisms can be markedly different from their bulk counterparts[13–16].

Despite a relative scarcity of experiments able to directly observe or measure dislocation nucleation[12,17–23], several recent studies combining atomistic simulations and transition state theory (TST) have provided insight into the nucleation mechanism under various loading conditions[24–27]. These simulations and experiments all unequivocally show that ultrahigh stresses near the theoretical strength are required for the nucleation process in pristine crystals, with a value that is generally much less sensitive to specimen size than for micrometre-sized crystals[14,28]. Furthermore, nucleation is strongly assisted by thermal fluctuations with corresponding atomically small activation volumes, in stark contrast to bulk crystals. These predictions have been corroborated by systematic temperature-dependent nanoindentation studies of face-centred cubic (FCC) crystals, albeit in a complex state of loading with large stress gradients and a presumed location for nucleation[17,29].

A striking implication from the small activation volumes is an intrinsic thermal uncertainty[13,17,30] that in experiments or device operation would manifest as a pronounced stochasticity of nucleation strengths, collapsing to a singular strength only in the athermal limit (0 K). This necessitates a statistical approach to any study and demands a non-deterministic approach to device design. No experimental study, to our knowledge, exists that fully characterizes the temperature-, size- and strain-rate-dependent nucleation process, with quantifiable mechanistic, energetic and kinetic deliverables, in defect-scarce materials subjected to spatially uniform stress states. Such a study would bolster our understanding of dislocations in crystals in their most embryonic state—at the point of nucleation.

Here, we aim to address these fundamental questions and gain a quantitative description of the energetic and kinetic barriers to surface dislocation nucleation in pristine crystals. We present systematic experimental tensile tests performed on defect-scarce single-crystalline Pd nanowhiskers (NWs), where dislocation nucleation is the predominant mechanism underlying plastic yielding. We have probed the quasi-static tensile response over a range of strain rates, sizes and temperatures, even approaching the athermal limit. With the aid of *in situ* tensile tests in the

---

[1]Department of Materials Science and Engineering, University of Pennsylvania, Philadelphia, Pennsylvania 19104, USA. [2]Max-Planck-Institut für Intelligente Systeme, D-70589 Stuttgart, Germany. *e-mail: gianola@seas.upenn.edu

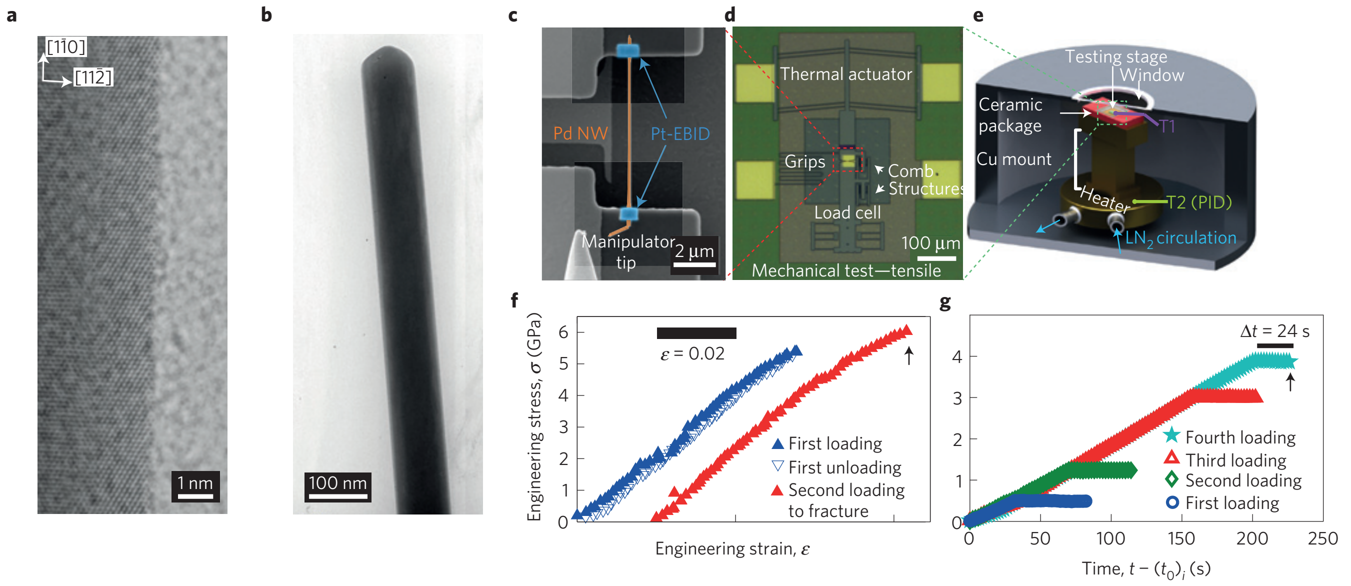

Figure 1 | Experimental method and verification of elasticity. a, High-resolution TEM micrograph of the surface morphology of a Pd NW along an edge between two facets. **b**, Bright-field TEM micrograph of a Pd NW. **c**, SEM micrograph of an individually manipulated NW mounted to the tensile testing stage grips. NW and EBID grips are artificially coloured for clarity. **d**, Optical micrograph of the MEMS tensile testing stage. **e**, Temperature testing configuration in the cryostat with the MEMS stage mounted in a ceramic package. A thermocouple mounted on the MEMS chip (T1) provides the sample temperature, and a Si diode sensor at the heat exchange base (T2) provides the reading to a PID temperature controller. **f**, Sample load–unload and subsequent fracture stress–strain curves for a single Pd NW, offset for clarity. **g**, Load-hold tests performed on a Pd NW to verify elasticity at high stresses. Time along the abscissa is with respect to the start time $(t_0)_i$ of the *i*th loading. Fractures in **f**,**g** occur where indicated by the black arrows.

TEM, we demonstrate a direct connection between incipient plasticity in our NWs and the nucleation of dislocations at free surfaces. Our measurements of over 60 individual NWs provide values for the energy barriers and kinetics governing dislocation nucleation, as well as insight into the highly probabilistic nature of dislocation nucleation.

Ultrahigh strength due to surface dislocation nucleation

The Pd NWs in this study are of high crystalline quality and defect-scarce owing to near-equilibrium growth conditions. Whereas no pre-existing unit dislocations were observed in any of our TEM investigations, a fraction of NWs from certain growth substrates contained a stacking fault along the axis of the NW, which is not expected to contribute to plastic deformation (see Methods and Supplementary Information). Individual specimens (Fig. 1a,b) were tested in tension using the set-up shown in Fig. 1c–e. Beginning with room temperature tensile behaviour, the Pd NWs exhibited large ultimate strengths as high as 7.8 GPa, over 200 times stronger than their bulk counterparts. In all Pd NWs tested, the elastic response became nonlinear at strains above 1% (ref. 31). Elastic deformation was confirmed by performing a series of load–unload tests to increasingly high strains, where on unloading the curve follows a nonlinear path back to zero load and strain (Fig. 1f). The elastic regime was terminated at strengths near the theoretical limit of Pd (ref. 32) by fracture or, in only four cases, a clearly distinguishable plastic flow regime in which the load remained approximately constant (see Supplementary Fig. 2). Additional load-hold testing provided further evidence of sustained elasticity and the absence of relaxation mechanisms at stresses well below the yield or fracture strengths. Figure 1g shows subsequent loadings of a single NW, which sustained a relatively constant load at increasingly higher levels of stress until fracture occurred during the final holding period. The finite duration of time (~24 s at 3.8 GPa) required for yield to occur under constant stress is consistent with a thermally activated mechanism and can be related to the expectation time for the first nucleation event.

The measured stress–strain response in our Pd NWs suggests that defect nucleation, and thus plastic deformation, is associated with the first measured deviations from elasticity. However, *in situ* TEM tests performed on other metallic nanostructures with non-zero defect density have shown that dislocation motion may still occur during what would otherwise seem to be elastic loading[33]. To verify the absence of dislocation motion or nucleation before yield or departure from elasticity in the stress–strain curve, we performed quantitative *in situ* TEM tensile tests on the Pd NWs.

Figure 2b–e shows a series of images captured during tensile testing of a Pd NW with a diameter of 60 nm, and Fig. 2f shows the corresponding stress–strain curve, which is described well by a nonlinear (quadratic) elastic relationship before fracture, as reported previously[31]. For this NW, diffraction contrast related to defects, such as dislocations and stacking faults, was not observed at the beginning of the test (Fig. 2b). Moreover, the NW remained defect-free during the test, for example, near the onset of nonlinear elasticity (Fig. 2c) and before the NW fractured (Fig. 2d) at a stress of 3.45 GPa. Subsequently, the NW abruptly fractured (Fig. 2e) in a shear mode (see Fig. 2g), with a shear plane determined to be $(1\bar{1}1)$, as the NW was oriented along $[1\bar{1}0]$ and observed in the [110] zone axis. Traces of stacking faults were observed parallel to the major $(1\bar{1}1)$ shear plane (and the equivalent $(\bar{1}11)$ plane), indicating that the shear fracture probably occurred by activation of a series of identical partial dislocations with $\mathbf{b} = [\bar{1}12]a/6$ (and the equivalent $\mathbf{b} = [1\bar{1}2]a/6$) from the side surfaces, which accorded well with previous atomistic simulations and *in situ* scanning electron microscope (SEM) measurements of Au NWs (ref. 34). Notably, no visible surface steps were evident during or after loading away from the fracture edge, which could arise from dislocation avalanches operating at speeds faster than our video rate. Figure 2h,i shows the stress–strain curve and fracture morphology of another defect-free Pd NW with a diameter of 64 nm, which was elastically loaded to 6.7 GPa and then fractured in a necking-like mode. Traces of stacking faults (or twinning planes) were also observed only near the fracture edges. A Schmid factor

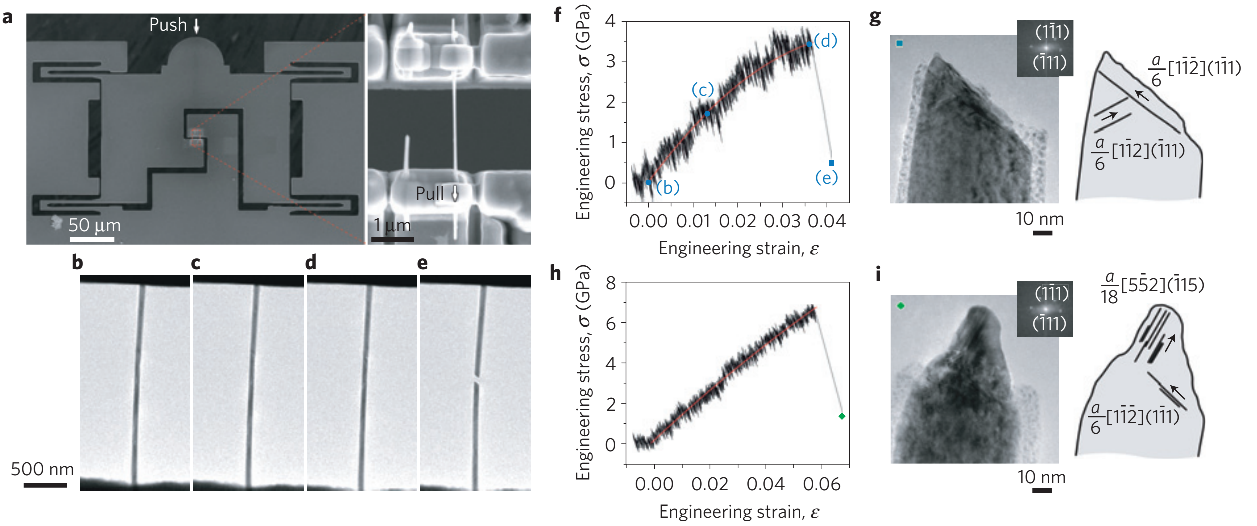

Figure 2 | *In situ* TEM tensile testing shows dislocation nucleation and failure occurring in short succession. a, Push-to-pull device with a secured NW. **b**–**e**, Sequential images from a single tensile test on a Pd NW. **f**, Stress–strain curve with a quadratic fit for the nonlinear response (red line) corresponding to the sequence in **b**–**e**. **g**, Fracture morphology showing stacking faults from equivalent slip systems. **h**, A second Pd NW of similar diameter tested under identical conditions. **i**, Fracture morphology of the second NW, showing sequential twinning on different slip systems. **g**,**i** were taken atomically resolved in high-resolution TEM mode parallel to the [110] crystal direction of Pd; the insets depict the fast Fourier transform (FFT) of the fracture areas respectively. The stacking fault planes are parallel and edge-on to the electron beam. No moiré patterns are observed that would evidence the presence of other stacking faults inclined to the electron beam. Detailed analyses of the observed slip plane traces can be found in the Supplementary Information.

analysis (see Supplementary Information) suggested that plastic deformation in this NW was mediated by partial dislocations (or twinning segments), operating in a primary slip system with $\mathbf{b}=[\bar{1}12]a/6$ on a $(1\bar{1}1)$ plane, followed by a secondary system with $\mathbf{b}=[5\bar{5}2]a/18$ on a $(\bar{1}15)$ plane with respect to the matrix orientation, which is equivalent to $\mathbf{b}=[1\bar{1}2]a/6$ on the $(\bar{1}11)$ plane in the primary twinned region. Such a plasticity mechanism mediated by multiple partial dislocations is consistent with previous studies of Au NWs grown in similar conditions[34], underscoring the role of dislocation nucleation from the surface of these NWs.

Our *in situ* TEM testing revealed that mobile dislocations were present neither inside the Pd NWs before testing nor during the entirety of the evidently elastic regime. However, clear evidence of late-stage plastic deformation strongly suggests that nucleation of dislocations gives rise to highly localized plastic deformation, followed rapidly by final fracture. Thus, the yield strengths measured in this study serve as a reasonable indicator of incipient plasticity and can be used for evaluating the critical stress for dislocation nucleation.

Effect of experimental parameters on nucleation

Probing the dependence of nucleation strength on testing parameters such as size, strain rate and temperature provided further quantitative insight to the underlying plasticity mechanism. To minimize convolution in the data, we define our benchmark conditions as NWs tested at room temperature (295 K) and an intermediate strain rate range ($\sim10^{-4}\,\mathrm{s}^{-1}$)—that is, all non-ambient temperature tests were performed at a strain rate in the $10^{-4}\,\mathrm{s}^{-1}$ range and all tests performed above or below $10^{-4}\,\mathrm{s}^{-1}$ were at room temperature. In Fig. 3, several characteristics of the tensile response, including ultrahigh yield strength in the gigapascal range and nonlinear elasticity at high strains, remain consistent among the different testing conditions. Elasticity at high strengths was again verified by performing load–unload tests before the fracture (see Supplementary Fig. 1).

Our results reveal the following trends for the nucleation strength. At room temperature, changes of two orders of magnitude in strain rate do not produce significant differences in the yield strengths. In contrast, spanning a temperature range of ~300 K demonstrates significant changes in yield strength. For the tensile test performed at 93 K, a yield strength as high as 5.8 GPa was attained. In contrast, the sample tested at 447 K fractured at a much lower strength of 2.8 GPa. This strong temperature dependence points to a deformation mechanism more thermally sensitive than the flow of pre-existing dislocations in FCC crystals[35], the strength for which would scale only weakly with the elastic constants (~4% versus 50% drop in strength for the given temperature range, for bulk and Pd NWs, respectively). Similar to the *in situ* TEM tests, the measured tensile response indicates a brittle-like behaviour whereas the fracture surface suggests otherwise. Fracture morphologies on all specimens indicate localized necking or shear deformation consistent with the previous *in situ* tests (Fig. 3c–g), suggesting that dislocation mechanisms govern plastic deformation over the entire range of tested strain rates and temperatures.

The experimental trends measured and illustrated in Fig. 3 are qualitatively consistent with theoretical predictions, both from semi-analytical models[26,36] and computational simulations[27,36,37], where strength is weakly dependent on strain rate but strongly dependent on temperature. The stochasticity of the measured nucleation strengths spanning several GPa under benchmark conditions for instance (Fig. 4), however, adds a statistical facet to the mechanism. Examining the measured strength as a function of size, either represented as diameter (Fig. 4a) or gauge length (Fig. 4b), shows a marginal size effect relative to this scatter over the tested range. This observation is likewise consistent with predictions[26,36] and other experiments[12,26] indicating weak size effects in defect-free metallic nanostructures. To determine the origin of the large scatter in measured strengths, we first systematically consider sources of experimental uncertainty, including effects such as variation in the applied strain rate, estimation of the cross-sectional area, and load bearing by a hydrocarbon-based contamination layer. We also consider any correlation of measured strength with fracture location and with the presence of the axially aligned stacking faults. As detailed in the Supplementary Information and indicated by error bars on our data, these cumulative uncertainties are substantially smaller than the measured scatter. We therefore attribute the stochasticity of

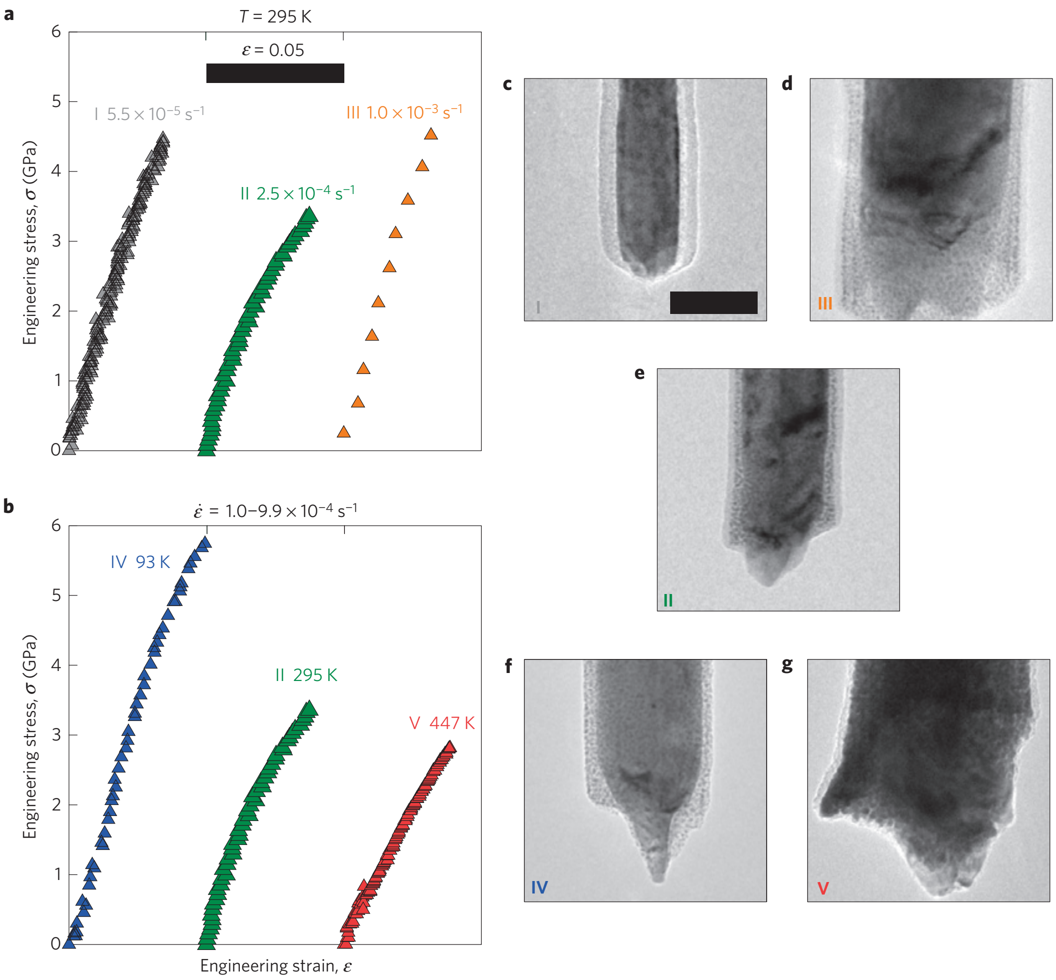

Figure 3 | Representative stress–strain behaviour shows strong temperature dependence of the nucleation strength and a similar deformation morphology irrespective of testing conditions. a,**b**, Stress–strain curves for tensile tests performed under various strain rate (**a**) and temperature (**b**) conditions. Stress-strain curves are offset for clarity with the strain quantity indicated by the bar in **a**. **c**–**g**, Corresponding postmortem fracture morphologies for the tensile tests labelled I–V in **a**,**b**. The nonlinear elastic response leading up to the nucleation event was found to be size-dependent in both the small strain (Young's) and higher order moduli owing to the increasing contribution of surface stresses with diminishing size coupled with the large lattice anharmonicity of Pd (ref. 31). All fracture micrographs are at the same magnification and correspond to the scale bar in **c** denoting 50 nm. We note that only fractured samples in IV (**f**) and V (**g**) are from the respective non-ambient temperature tests in **b**, but samples I (**c**), II (**e**) and III (**d**) were tested under the same conditions as the corresponding tests shown in **a**. The hydrocarbon-based coatings are the result of NW manipulation before and after tensile testing; a detailed analysis of its influence is presented in the Supplementary Information.

our measurements to a probabilistic thermally activated deformation process.

Examining the full data set of over 60 NWs, we find that whereas tensile tests performed at various strain rates do not show a rate dependence that rises above the scatter (Fig. 5a), the nucleation strength is found to vary significantly with temperature. Comparing the mean strength values at the tested temperature limits shows a strength reduction of nearly 6 GPa over a 350 K increase in temperature (Fig. 5b). This large monotonic decrease in strength with increasing temperature, associated with dislocation-mediated deformation, unambiguously points to a thermally activated process. As well as the mean strength, the measured scatter band is also a function of temperature, with the largest variation emerging near room temperature and reducing in both the athermal (with thermal fluctuations absent) and high-temperature (bounded by zero stress) limits.

Discussion and theoretical comparisons

We analyse these temperature-dependent distributions of nucleation strength to evaluate the thermal activation parameters associated with surface dislocation nucleation. From TST, the rate of dislocation nucleation ν is expressed as:

$$\nu = N\nu_0 \exp\left(-\frac{\Delta G_{\mathrm{act}}(\sigma,T)}{k_{\mathrm{B}}T}\right) \tag{1}$$

where ν_0 is the attempt frequency, N is the number of equivalent nucleation sites, $\Delta G_{\mathrm{act}}(\sigma,T)$ is the activation free energy and k_{B} is the Boltzmann constant. To directly compare our experimental results against the proposed temperature and stress dependencies of ΔG_{act}, we adopt the simple form for the activation energy following the work of refs 36–38:

$$\Delta G_{\mathrm{act}}(\sigma,T) = \Delta U_{\mathrm{act}}\left(1-\frac{T}{T_{\mathrm{m}}}\right)\left(1-\frac{\sigma}{\sigma_{\mathrm{ath}}}\right)^{\alpha} \tag{2}$$

Here, σ_{ath} is the athermal strength, ΔU_{act} is the zero-temperature, zero-stress activation energy, and both T_{m} and α are constants governing the temperature and stress dependencies, respectively[36]. Mechanistically, α is related to the particular obstacle that must be overcome during the thermally activated process. A strong stress dependence has been proposed ($\alpha \approx 4$) on the

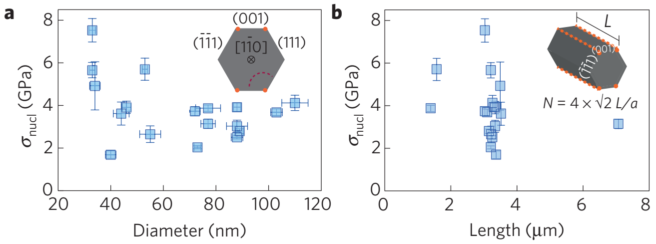

Figure 4 | Weak size dependence of nucleation strength. a,**b**, Nucleation strengths measured in Pd NWs across a range of diameters (**a**) and gauge lengths (**b**) at $T = 295$ K and strain rates of the order of 10^{-4} s^{-1}. Schematics in the upper right-hand corners illustrate predicted nucleation of a dislocation from a corner site in **a** and the relationship between length L and number of equally viable nucleation sites N for lattice parameter a in **b**. Viable nucleation sites are indicated by orange circles or orange dotted lines. Horizontal error bars in **a** correspond to the standard deviation of at least ten measurements of diameter; the length of each sample was measured only once, so there are no horizontal error bars in **b**. Vertical error bars in **a**,**b** were calculated from the uncertainties in cross-section (diameter) and load measurements. See Supplementary Information for more details.

basis of calculations of the activation energy for simulations of heterogeneous corner dislocation nucleation in a Cu NW under tension[36]. We thus compute the full temperature-dependent nucleation strength distributions for both $\alpha = 1$ (as has been assumed for dislocation nucleation in refs 30,39) and $\alpha = 4$ to draw comparisons to our experiments (for details of these derivations, see the Supplementary Information).

We employ the approach taken in ref. 40, and substitute equation (2) for $\alpha = 4$ into equation (1) to define a cumulative probability distribution function $F(\sigma)$ (Supplementary Equations 4 and 7); we fit this to the experimental data to obtain σ_{ath}, the Arrhenius prefactor $N\nu_0$, and the Helmholtz free energy of activation $\Delta F_{\text{act}}(T) = \Delta U_{\text{act}}(1 - T/T_{\text{m}})$ (Fig. 5c). Using nonlinear least squares regression, we obtain $\sigma_{\text{ath}} = 7.08 \pm 0.02$ GPa, $N\nu_0 = 0.065 \pm 0.003$ s^{-1}, and $\Delta F_{\text{act}}(T) = 0.236 \pm 0.009$ eV. Assuming T_{m} is half the bulk melting temperature of Pd ($T_{\text{m}} = 914$ K), we then calculate $\Delta U_{\text{act}} = 0.328$ eV.

Using these values, we calculate the most probable critical nucleation strength σ_{c} at 295 K for $\alpha = 4 (\alpha = 1)$ to be 3.44 GPa (5.85 GPa), which corresponds to an activation energy and volume $\Delta G_{\text{act}} = 0.016\,\text{eV}(0.048\,\text{eV})$ and $\Omega = 2.70\,\text{Å}^3 = 0.13b^3(4.79\,\text{Å}^3)$, respectively, where b is the magnitude of the full FCC Burgers vector. In comparison, simulations of surface dislocation nucleation in a Cu NW in tension yield $\Delta G_{\text{act}} = 0.39$ eV and $\Omega = 5b^3$ at the same temperature and fraction of the athermal strength[36], at least an order of magnitude higher than those from our experiments on Pd NWs. Likewise, our calculated maximum activation entropy for Pd is $4.17k_{\text{B}}$, implying a non-negligible contribution to the nucleation rate ($\sim \exp(\Delta S_{\text{act}}/k_{\text{B}})$). This compares with calculations giving $9k_{\text{B}}$ and $48k_{\text{B}}$ for homogeneous nucleation in Cu under constant strain and stress, respectively[27]. Considering the low activation energies deduced from our experiments, it is plausible that certain pre-existing flaws that go undetected, such as vacancies and atomic surface steps, could lower the nucleation barrier with respect to an ideal crystal. In Pd, the vacancy migration energy is reported as 0.82 eV, and the formation energy and volumes as 1.4 eV and $0.24b^3$, respectively[41]; given these larger barriers, it is unlikely that they contribute significantly to the experimentally observed behaviour. On the other hand, surface self-diffusion on {111} Pd facets (predominant on the surfaces of our NW specimens) has an activation energy of 0.031 eV (ref. 42), comparable to the energy we measure and consistent with an atomically sized activation volume. The striking implication is, thus, that surface diffusion, mediated by stresses near the ideal limit, may serve as a precursor mechanism to displacive ones that produce dislocation content within the crystal[15]. This notion is also consistent with recent observations of stress-assisted plastic deformation in Ag nanoparticles, where diffusive plasticity led to large pseudoelastic response[16]. In addition, pre-existing flaws such as surface steps are plausible in experimental specimens: simulation studies have shown that the activation parameters for nucleation can change significantly in the presence of such defects[36,43]. Their role, however, hinges on the configuration of these flaws relative to the applied stress and other defects. For instance, simulations of kinks on existing surface steps were shown not to influence the elastic limit in Al (ref. 43). Ultimately, the contributions from intrinsic (thermal fluctuations) and extrinsic (variations in surface quality from specimen to specimen) stochasticity could presumably be discerned by testing at even lower temperatures near 0 K; thus, the activation parameters we report here are effective ones.

The probabilistic nature of surface dislocation nucleation instantly emerges when comparing our full data set with computed temperature-dependent probability distribution function (PDFs). The PDF at each temperature is shown in Fig. 6 and normalized by its maximum probability to highlight the trajectory of σ_{c} over temperature. We compare our data against cases of both strong

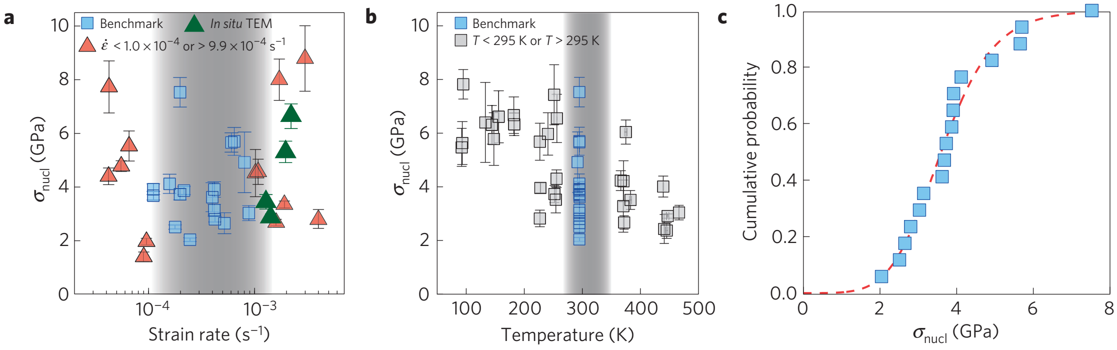

Figure 5 | Strain rate and temperature dependence, and statistical analysis of benchmark experiments. a,**b**, Nucleation strength in Pd NWs measured for different strain rates (**a**)—including results from the *in situ* TEM tests (green triangles)—and different temperatures (**b**). Blue squares and grey shading represent measurements at 295 K and strain rates of the order of 10^{-4} s^{-1}, as shown in Fig. 4. Measurements outside of these benchmark conditions are indicated by a different colour or symbol (triangles for strain rate outside 10^{-4} s^{-1}, black and grey for T outside 295 ± 5 K). Vertical error bars in **a**,**b** were calculated from the uncertainties in cross-section (diameter) and load measurements. See Supplementary Information for more details. **c**, Cumulative probability for measured yield strengths. The dotted red line is a fit for the analytically derived cumulative distribution function $F(\sigma)$.

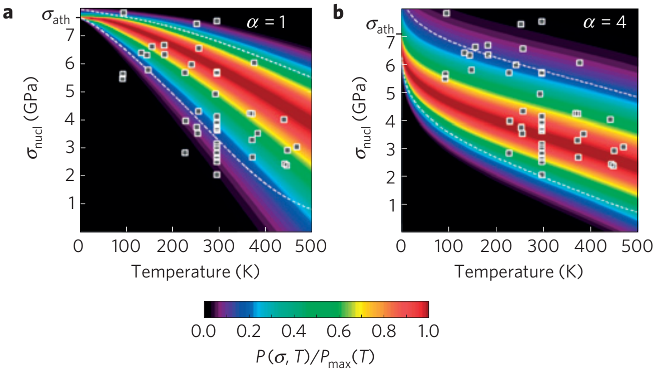

Figure 6 | Comparison between the experimental temperature-dependent nucleation strength distribution and the analytical model for the probability distribution. a,**b**, Normalized PDF maps for $\alpha = 1$ (**a**) and $\alpha = 4$ (**b**) are overlaid with measured nucleation stress (grey squares) at strain rates of the order of 10^{-4} s^{-1} (data points same as in Fig. 5b). The respective values for σ_{ath} are indicated on the vertical axes. Probability values $P(\sigma, T)$ are normalized with respect to the maximum probability $P_{max}(T)$ at each temperature; thus, each vertical slice represents the probability distribution at a given temperature, which collapses to a deterministic value in the athermal limit. The dashed contour lines represent the 5th (lower) and 95th (upper) percentile nucleation stresses.

($\alpha = 4$) and weak ($\alpha = 1$) stress dependence of the activation energy. Both models capture the strong temperature dependence of the mean nucleation strength and, more remarkably, of the non-monotonic scatter in probable nucleation strengths observed in experiment. Contour lines indicating the 5th and 95th percentile nucleation strength at each temperature show that the influence of α is most evident at low temperatures, particularly in the athermal limit, suggesting that further measurements at ultralow temperatures would be a promising avenue to gain further insight into the details of surface nucleation.

In summary, we have quantified the energetic and kinetic barriers to surface dislocation nucleation-mediated plastic deformation in uniformly strained NWs. Our results provide new insight into a class of defects that affect material properties and device performance in a host of technological sectors. We find that the plastic deformation is mediated by surface dislocation nucleation at ultrahigh stresses (athermal strength ~8% of the shear modulus) near the theoretical limit of strength, representing the highest ever measured in an FCC metal. Our experiments uncover a strong temperature dependence of strength and its associated scatter, well in excess of what is observed in bulk FCC metals and suggesting a surface diffusion mechanism as the rate-limiting step needed to promote displacive activity. Our results can ultimately be used to predict the nucleation behaviour under extreme conditions and inform probabilistic models and device design strategies employing nanoscale materials.

Methods

Methods and any associated references are available in the online version of the paper.

Received 20 February 2015; accepted 2 April 2015;
published online 18 May 2015

References

1. Hirsch, P. B., Horne, R. W. & Whelan, M. J. LXVIII Direct observations of the arrangement and motion of dislocations in aluminium. *Phil. Mag.* **1,** 677–684 (1956).
2. Taylor, G. I. The mechanism of plastic deformation of crystals. Part I. Theoretical. *Proc. R. Soc. Lond. A* **145,** 362–387 (1934).
3. Orowan, E. Zur Kristallplastizität. I. *Z. Phys.* **89,** 605–613 (1934).
4. Polanyi, M. Über eine Art Gitterstörung, die einen Kristall plastisch machen könnte. *Z. Phys.* **89,** 660–664 (1934).
5. Frank, F. C. The influence of dislocations on crystal growth. *Discuss. Faraday Soc.* **5,** 48–54 (1949).
6. Hirth, J. P. & Pond, R. C. Steps, dislocations and disconnections as interface defects relating to structure and phase transformations. *Acta Mater.* **44,** 4749–4763 (1996).
7. Swann, P. R. Dislocation substructure vs transgranular stress corrosion susceptibility of single phase alloys. *Corrosion* **19,** 102t–114t (1963).
8. Farvacque, J. L., Douehan, J. C., von Alpen, U. & Gmelin, E. Screw-dislocation-induced scattering processes and acceptor states in Te. *Phys. Status Solidi* **79,** 763–773 (1977).
9. Lee, M. L., Fitzgerald, E. A., Bulsara, M. T., Currie, M. T. & Lochtefeld, A. Strained Si, SiGe, and Ge channels for high-mobility metal-oxide-semiconductor field-effect transistors. *J. Appl. Phys.* **97,** 011101 (2005).
10. Nam, S-W. *et al.* Electrical wind force-driven and dislocation-templated amorphization in phase-change nanowires. *Science* **336,** 1561–1566 (2012).
11. Wagner, R. S. & Ellis, W. C. Vapor–liquid–solid mechanism of single crystal growth. *Appl. Phys. Lett.* **4,** 89–90 (1964).
12. Richter, G. *et al.* Ultrahigh strength single crystalline nanowhiskers grown by physical vapor deposition. *Nano Lett.* **9,** 3048–3052 (2009).
13. Zhu, T. & Li, J. Ultra-strength materials. *Prog. Mater. Sci.* **55,** 710–757 (2010).
14. Greer, J. R. & De Hosson, J. T. M. Plasticity in small-sized metallic systems: Intrinsic versus extrinsic size effect. *Prog. Mater. Sci.* **56,** 654–724 (2011).
15. Li, J. *et al.* Diffusive molecular dynamics and its application to nanoindentation and sintering. *Phys. Rev. B* **84,** 054103 (2011).
16. Sun, J. *et al.* Liquid-like pseudoelasticity of sub-10-nm crystalline silver particles. *Nature Mater.* **13,** 1007–1012 (2014).
17. Schuh, C. A., Mason, J. K. & Lund, A. C. Quantitative insight into dislocation nucleation from high-temperature nanoindentation experiments. *Nature Mater.* **4,** 617–621 (2005).
18. Oh, S. H., Legros, M., Kiener, D. & Dehm, G. *In situ* observation of dislocation nucleation and escape in a submicrometre aluminium single crystal. *Nature Mater.* **8,** 95–100 (2009).
19. Zheng, H. *et al.* Discrete plasticity in sub-10-nm-sized gold crystals. *Nature Commun.* **1,** 144 (2010).
20. Jennings, A. T., Li, J. & Greer, J. R. Emergence of strain-rate sensitivity in Cu nanopillars: Transition from dislocation multiplication to dislocation nucleation. *Acta Mater.* **59,** 5627–5637 (2011).
21. Lu, Y., Song, J., Huang, J. Y. & Lou, J. Surface dislocation nucleation mediated deformation and ultrahigh strength in sub-10-nm gold nanowires. *Nano Res.* **4,** 1261–1267 (2011).
22. Bei, H., Gao, Y., Shim, S., George, E. & Pharr, G. Strength differences arising from homogeneous versus heterogeneous dislocation nucleation. *Phys. Rev. B* **77,** 060103 (2008).
23. Gerberich, W. W., Nelson, J. C., Lilleodden, E. T., Anderson, P. & Wyrobek, J. T. Indentation induced dislocation nucleation: The initial yield point. *Acta Mater.* **44,** 3585–3598 (1996).
24. Li, J., Van Vliet, K. J., Zhu, T., Yip, S. & Suresh, S. Atomistic mechanisms governing elastic limit and incipient plasticity in crystals. *Nature* **418,** 307–310 (2002).
25. Warner, D. H. & Curtin, W. A. Origins and implications of temperature-dependent activation energy barriers for dislocation nucleation in face-centered cubic metals. *Acta Mater.* **57,** 4267–4277 (2009).
26. Jennings, A. T. *et al.* Modeling dislocation nucleation strengths in pristine metallic nanowires under experimental conditions. *Acta Mater.* **61,** 2244–2259 (2013).
27. Ryu, S., Kang, K. & Cai, W. Entropic effect on the rate of dislocation nucleation. *Proc. Natl Acad. Sci. USA* **108,** 5174–5178 (2011).
28. Uchic, M. D., Dimiduk, D. M., Florando, J. N. & Nix, W. D. Sample dimensions influence strength and crystal plasticity. *Science* **305,** 986–989 (2004).
29. Bahr, D. F., Wilson, D. E. & Crowson, D. A. Energy considerations regarding yield points during indentation. *J. Mater. Res.* **14,** 2269–2275 (2011).
30. Ngan, A. H. W., Zuo, L. & Wo, P. C. Size dependence and stochastic nature of yield strength of micron-sized crystals: A case study on Ni3Al. *Proc. R. Soc. Lond. A* **462,** 1661–1681 (2006).
31. Chen, L., Richter, G., Sullivan, J. & Gianola, D. Lattice anharmonicity in defect-free Pd nanowhiskers. *Phys. Rev. Lett.* **109,** 125503 (2012).
32. Kamran, S., Chen, K. & Chen, L. *Ab initio* examination of ductility features of fcc metals. *Phys. Rev. B* **79,** 024106 (2009).
33. Chisholm, C. *et al.* Dislocation starvation and exhaustion hardening in Mo alloy nanofibers. *Acta Mater.* **60,** 2258–2264 (2012).
34. Sedlmayr, A. *et al.* Existence of two twinning-mediated plastic deformation modes in Au nanowhiskers. *Acta Mater.* **60,** 3985–3993 (2012).

35. Masumoto, H., Saitô, H. & Kadowaki, S. Young's modulus of single crystals of palladium at high temperatures. *Sci. Rep. Res. Inst. Tohoku Univ. A* **19,** 294–303 (1967).
36. Zhu, T., Li, J., Samanta, A., Leach, A. & Gall, K. Temperature and strain-rate dependence of surface dislocation nucleation. *Phys. Rev. Lett.* **100,** 025502 (2008).
37. Ryu, S., Kang, K. & Cai, W. Predicting the dislocation nucleation rate as a function of temperature and stress. *J. Mater. Res.* **26,** 2335–2354 (2011).
38. Kocks, U. F., Argon, A. & Ashby, M. F. *Thermodynamics and Kinetics of Slip* (Argonne National Laboratory, 1973).
39. Mason, J., Lund, A. & Schuh, C. Determining the activation energy and volume for the onset of plasticity during nanoindentation. *Phys. Rev. B* **73,** 054102 (2006).
40. Zuo, L. & Ngan, A. H. W. Molecular dynamics study on compressive yield strength in Ni_3Al micro-pillars. *Phil. Mag. Lett.* **86,** 355–365 (2006).
41. Foiles, S., Baskes, M. & Daw, M. Embedded-atom-method functions for the fcc metals Cu, Ag, Au, Ni, Pd, Pt, and their alloys. *Phys. Rev. B* **33,** 7983–7991 (1986).
42. Liu, C. L., Cohen, J. M., Adams, J. B. & Voter, A. F. EAM study of surface self-diffusion. *Surf. Sci.* **253,** 334–344 (1991).
43. Brochard, S., Hirel, P., Pizzagalli, L. & Godet, J. Elastic limit for surface step dislocation nucleation in face-centered cubic metals: Temperature and step height dependence. *Acta Mater.* **58,** 4182–4190 (2010).

Acknowledgements

This research was supported by the National Science Foundation through a CAREER Award #DMR-1056293. We thank S. Terrab (University of Colorado Boulder) for technical expertise and project support. We are also grateful to V. Vitek for critical reading of our manuscript and insightful comments. The authors also thank the support of the staff and facilities at the Penn Nanoscale Characterization Facility at the University of Pennsylvania. This work was performed, in part, at the Center for Integrated Nanotechnologies, a US Department of Energy, Office of Basic Energy Sciences user facility. Sandia National Laboratories is a multi-programme laboratory managed and operated by Sandia Corporation, a wholly owned subsidiary of Lockheed Martin Corporation, for the US Department of Energy's National Nuclear Security Administration under contract DE-AC04-94AL85000.

Author contributions

L.Y.C. and D.S.G. designed the experiments. L.Y.C. implemented the low-temperature testing set-up. L.Y.C., M-r.H. and J.S. conducted mechanical experiments and material characterization. G.R. synthesized the materials and conducted material characterization. L.Y.C. and D.S.G. developed the analytical model and performed analysis of the data. D.S.G. supervised the work. L.Y.C. and D.S.G. wrote the initial manuscript with input from all authors. All authors contributed to discussion of the results, provided input on the manuscript, and approved the final version.

Additional information

Supplementary information is available in the online version of the paper. Reprints and permissions information is available online at www.nature.com/reprints. Correspondence and requests for materials should be addressed to D.S.G.

Competing financial interests

The authors declare no competing financial interests.

Methods

Sample synthesis and characterization. Single-crystalline Pd NWs were grown by thermal evaporation at 1,200 °C onto (001)-$SrTiO_3$ or (0001)-Al_2O_3 substrates at elevated temperature under ultrahigh vacuum conditions. Further details of the growth procedure and mechanism are documented elsewhere[12]. The orientation was confirmed by electron diffraction analysis on at least ten NWs with diameters $30 < d < 150$ nm from each substrate before testing. The bottom-up growth at near-equilibrium conditions resulted in distinct surface facets, and the NWs showed no evidence of taper or visible roughness on the surfaces (Fig. 1a). High-resolution scanning transmission electron microscopy (STEM) verified the absence of a native oxide layer on the NWs. As both high temperature (>1,000 K) and oxygen partial pressure are required to form oxide layers on Pd (ref. 31), these NWs were expected to remain oxide-free during testing at elevated temperatures. For Pd NWs grown on the $SrTiO_3$ substrate (35% of entire data set), TEM imaging showed no visible pre-existing defects such as dislocations or vacancy clusters (Fig. 1b). For the remaining NWs grown on Al_2O_3, about half of the specimens examined had stacking faults (~30% of entire data set) along the axis, whereas the remainder were defect-free. Because the stacking fault is along the NW axis, its resolved shear stress is zero. Postmortem imaging in the TEM confirmed that the stacking faults remained in the NW even after fracture, and the nucleation strength distributions from data sets containing defect-free NWs and those containing stacking faults were not statistically distinct (see Supplementary Information for full analysis).

Tensile testing and temperature control. Individual NWs were harvested using a nanomanipulator directly from the growth substrate and attached onto the microelectromechanical systems (MEMS) tensile testing stage using Pt-containing electron beam-induced deposits (EBID; Fig. 1c). The stress–strain response during tensile loading was measured by tracking the displacements of the load cell and actuator (Fig. 1d) using digital image correlation. These displacements were tracked either by EBID fiducial markers placed near the sample and on the grips for SEM images or by comb features under the optical microscope[44]. Although the compliance of the EBID grips is known to affect the apparent strain measurement during tensile testing (which is corrected for), the compliance does not influence the load—and therefore strength—measurements that are the focus of this study[33]. The MEMS stage was set in a ceramic electronics package that enabled easy transport between SEM and optical set-ups as well as connection to an external power supply for operating the actuator. Owing to the low thermal mass, the stage could be heated or cooled uniformly. The package within the cryostat was thermally coupled to the heat exchanger for the cryogen (LN_2; Fig. 1e). Elevated temperatures up to 475 K were achieved with a cartridge heater connected to a PID temperature controller. The temperature reported at the sample was measured from a thermocouple attached to the tensile stage substrate. Pd NWs were tested at strain rates in the range of $10^{-5}\ s^{-1}$ to $10^{-3}\ s^{-1}$ and nominal temperatures from 77 to 475 K. Further details of the set-up, including temperature control and stability, can be found in ref. 44.

***In situ* TEM experiments—set-up.** Similar to the above manipulation procedure, individual Pd NWs were aligned and mounted on a MEMS fabricated push-to-pull (PTP) device[33] (Fig. 2a). A PI-95 TEM PicoIndenter from Hysitron[45] was then used to push the semicircle head of the PTP device with a diamond flat punch indenter at a constant displacement rate of $4\ nm\ s^{-1}$, pulling the bridged Pd NW in tension. Experiments were performed in a JEOL 2100 TEM. Load and displacement data were recorded and converted to the stress–strain response of Pd NWs based on a procedure similar to refs 33,44.

The resolution of the recorded load displacement signals was <0.2 μN and <1.0 nm, respectively. The spring constant of empty PTP device, that is, the four springs loaded in parallel with the tested NW, was measured after NW fracture. The force applied to the NW was thus determined by subtracting the elastic force of the PTP device from the total load. The cross-section of the NW was approximated as a circle, with the diameter taken as the average of projective widths with the specimen holder tilted at 0° and 30°. The initial gauge length of the NW was measured by SEM as the distance between the two Pt grips. The elongation of the NW was considered to be uniform before fracture and simply equal to the displacement of indenter, as the compliance of Pt grips has been shown to be negligible for the NW diameters tested by *in situ* TEM (refs 31,33).

References

44. Murphy, K. F., Chen, L. Y. & Gianola, D. S. Effect of organometallic clamp properties on the apparent diversity of tensile response of nanowires. *Nanotechnology* **24,** 235704 (2013).
45. Minor, A. M. *et al.* A new view of the onset of plasticity during the nanoindentation of aluminium. *Nature Mater.* **5,** 697–702 (2006).

nature materials
SUPPLEMENTARY INFORMATION
DOI: 10.1038/NMAT4288

Measuring surface dislocation nucleation in defect-scarce nanostructures

Lisa Y. Chen[1], Mo-rigen He[1], Jungho Shin[1], Gunther Richter[2], Daniel S. Gianola[1,a]

[1]Department of Materials Science and Engineering, University of Pennsylvania, Philadelphia,
PA 19104, USA
[2]Max-Planck-Institut für Intelligente Systeme, D-70589 Stuttgart, Germany

---

[a] Correspondence and requests for materials should be addressed to D.S.G. (email: gianola@seas.upenn.edu)

Tensile Testing Procedure and Stress-strain Responses

In order to verify elastic deformation up to the first measurable plastic event, Pd NWs were subjected to successive load-unload tests to increasingly higher displacements until fracture.

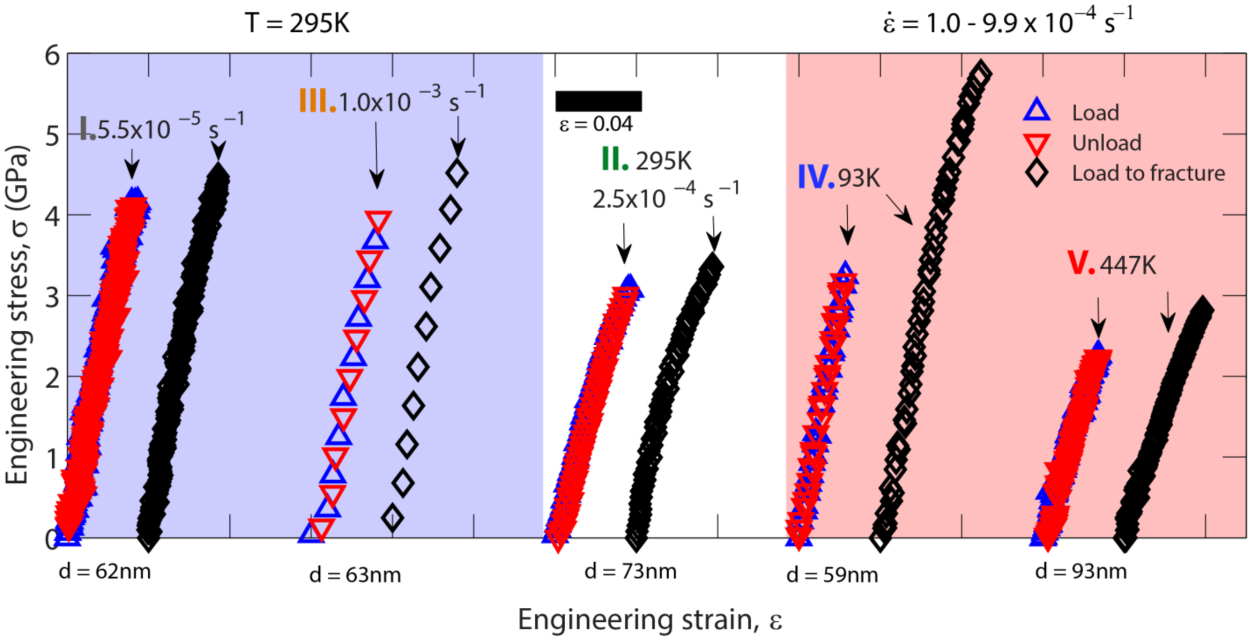

Figure S1. Load-unload and load-to-fracture stress-strain curves representing different testing condition regimes for temperature and strain rate. The roman numerals correspond to those in Fig. 3 in the main paper.

Figure S1 shows the typical testing sequence for several conditions. The red and blue symbols correspond to the elastic loading and unloading, respectively. The black symbols show the subsequent experiments taken to fracture to determine the dislocation nucleation stress as described in the main text.

Only 4 of over 60 samples tested and included in this study exhibited clear indication of a plastic flow regime in the stress-strain response. All 4 specimens were tested at room temperature either at benchmark conditions or low strain rates ($< 10^{-4}$ s^{-1}). The elastic-to-plastic transitions were demarcated by a clear yield point, and plastic flow proceeded at roughly constant load to fracture (Fig. S2); therefore, in this and similar cases, we report the yield strength as the nucleation strength. Our microstructural characterization of these specimens exhibiting plastic flow showed no significant differences from the remainder of the experiments; thus we treat the specimens as nominally similar.

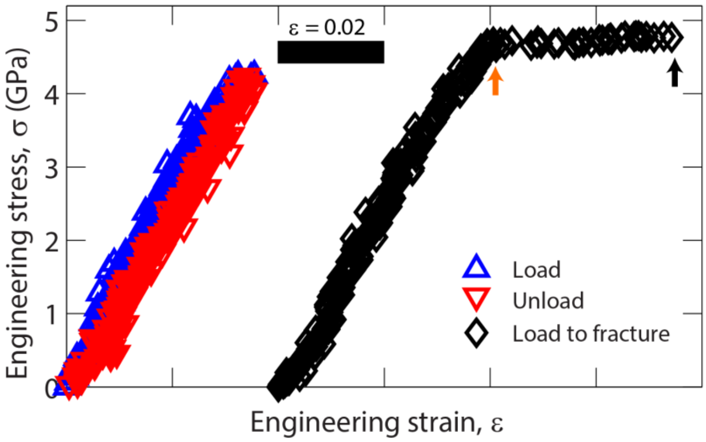

Figure S2. Representative stress-strain response in specimens exhibiting plastic flow after yielding. Flow at roughly constant load was sustained until fracture (black arrow). The reported nucleation strength is the yield point (orange arrow).

Contributions to Scatter Due to Experimental Uncertainties

Given the intrinsic stochastic nature of surface dislocation nucleation, it is important to address the influence of other potential contributors of experimental scatter or error in the measurement of nucleation strengths prior to conducting our full statistical analysis. We consider five primary sources of uncertainty: error due to variation in applied strain rate; errors in measurement of the NW cross-section; load-bearing by the hydrocarbon-based coating; correlation between measured strength and fracture location; and correlation between measured strength and microstructure.

The error owing to variation in strain rate introduced in the benchmark stress measurement can manifest in two manners: the deterministic error from including a range of strain rates within the benchmark data ($1.0\text{x}10^{-4}$ $\text{s}^{-1} < \dot{\varepsilon} < 9.9\text{x}10^{-4}$ s^{-1}), and the experimental uncertainty for individual tests stemming from imaging and time resolution (time elapsed between image captures). These contributions can be calculated by using the approximated relationship between the critical nucleation stress and strain rate from Zhu et al.[1] The influence of strain rate on the strength measurements benchmark conditions is $\Delta\sigma = \left(\frac{k_b T}{\Omega}\right)^2 \frac{N\nu_0}{E\dot{\varepsilon}} \Delta\dot{\varepsilon}$. For the deterministic error contribution, using the parameters from the $\alpha = 4$ case and a maximum difference from the average strain rate of $\Delta\dot{\varepsilon} = 5.0\text{x}10^{-4}$ s^{-1}, the upper bound for the increase in mean strength is 1.6 MPa. This very small predicted change in the mean strength is consistent with the negligible strain rate dependence in Fig. 5a in the main paper. For a given strength measurement the average uncertainty in the reported strain rate for the benchmark data is $\Delta\dot{\varepsilon} = 5.5\text{x}10^{-5}$ s^{-1}. This yields an uncertainty in the strength measurement of 0.18 MPa, which is orders of magnitude lower than the observed scatter.

For many NW specimens, the cross-sectional shape can be examined after fracture by either using the nanomanipulator to bend up the fractured ends or to use focused ion beam to cross-section the NW at the EBID contact[2]. The cross-section of most Pd NW specimens is hexagonal (truncated rhombic) and consistent with Wulff shape predictions. To assess the error from assuming a circular-cross section based on measurements of the projected effective diameter, we calculated the difference in area between a circle and a regular hexagon. This circular approximation for area can underestimate the true area by 10% or overestimate by as much as 21%, depending on the azimuthal viewing angle. In some cases, a more oblong cross-section had been observed with an aspect ratio of about 2:1 and approximated as an ellipse. The error is bounded by the difference between an ellipse and a rectangle of the same dimensions, which is approximately 21%. For the average NW diameter of 60 nm or equivalent-area cross-section, this would result in an average deviation in measured strength of about 10%, which is comparable to the error from imaging resolution reflected in the current error bars.

Post-manipulation imaging of both postmortem and pristine (not tested) Pd NWs indicate the universal presence of a hydrocarbon-based contamination layer ranging anywhere between 1-20 nm thick. Contamination of the pristine NW surfaces during electron microscopy imaging results from two primary sources: interaction of the electron beam with organic molecules in the chamber[3,4], and the organometallic gas precursor used to create the Pt-EBID contacts necessary for mechanical testing. The latter can occur from delocalization of the primary electron beam, decomposition of the precursor gas owing to secondary electron scattering events away from the primary beam, or diffusion of the deposited species along the NW. Based on stiffness measurements in unreinforced hydrocarbon deposition of 34-60 GPa[5], the coating volume fraction can be as high as 65% and the apparent load bearing of the NW would be predicted to increase as much as 80% for diameters as small as 30 nm. To evaluate the effect of load-bearing, we performed load-unload tests on samples with increasing amounts of coating and measured the apparent stiffness (load borne by NW cross-section only). For one sample, coating thickness volume fraction increased from 22% to 41% due to long dwell-time imaging in the SEM, where contaminants pre-existing in the chamber decomposed under the electron beam. In another case, we employed both long dwell-time imaging and imaging with the Pt-EBID source over the entire gage to mimic deposition conditions during manipulation, increasing the volume fraction from 26% to 34%. In both cases, we found no increase in apparent load borne by the NW beyond the uncertainty due to imaging noise (~0.08 μN or ~20 MPa). This suggests that even in the most extreme cases of the smallest NW diameters, the hydrocarbon-based coating does not significantly affect our strength measurements.

The uniaxial testing geometry and the high crystal quality of the Pd NWs we employ enable equal likelihood of nucleation at any site along the tested gage length. In practice (and in macroscopic testing), fracture towards the middle of the gage is most easily interpreted because this can be exclusively attributed to the response of the material. In contrast, fracture near the grips or "end fracture" may indicate geometric weakening owing to stress concentrations or misalignment-induced bending, resulting in lower measured strengths. In order to test a null hypothesis that σ_{nucl} is not significantly correlated with fracture location, we have separated the benchmark data in two groups (Table S1). Within our "benchmark" data, there are 11 wires that fractured within the gage section and 6 that fractured at or near the grip (Fig. S3) (this proportion of about 30% end fractures is also representative of the entire data set). The two groups were analyzed with basic statistical methods and results are shown below (Table S1). Even though the average strength of wires fractured in the middle was higher by ~1 GPa, a basic t-test shows the difference between these groups to be statistically insignificant (p-value of 0.09).

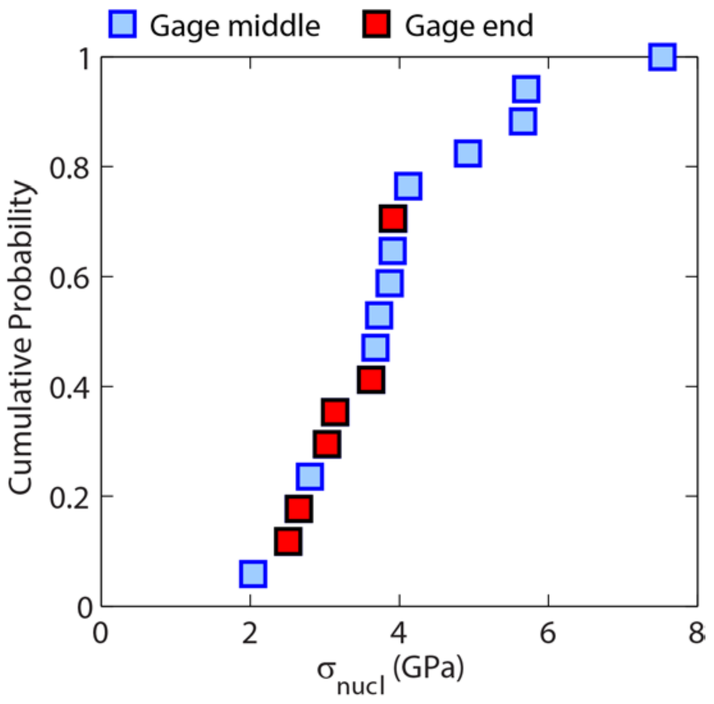

Figure S3. Experimental CDF distinguishing the fracture location for each specimen and its corresponding measured strength.

Table S1. Statistical parameters for two groups representing different fracture locations.

	Middle fracture	**End fracture**
Number of samples	11	6
Average σ_{nucl} (GPa)	4.36	3.05
Standard deviation (GPa)	1.52	0.55

The tested Pd NWs were either completely free of defects or contained stacking faults aligned along the axis of the NW. While the stacking fault itself is not expected to be activated during tensile testing since there is no resolved shear stress along the fault, and indeed has been observed to remain in the NW after fracture, it could have an influence on the nucleation of a dislocation via a back stress or by intersecting with corner nucleation sites, creating an atomically modified corner geometry. No such defects were observed in NW specimens harvested from the $SrTiO_3$ substrate, but about 50% of the NWs from Al_2O_3 investigated in the TEM possessed such defects. Among the benchmark data, 12 samples were from SrTiO3 and the remaining 5 are from Al_2O_3 (Fig. S4). Our t-test results indicate that the difference between the two groups is not statistically significant (p-value of 0.30). This suggests that any difference in strength related to the presence of the stacking fault defect is dwarfed by the thermal uncertainty of the nucleation process, which is the primary objective of this work.

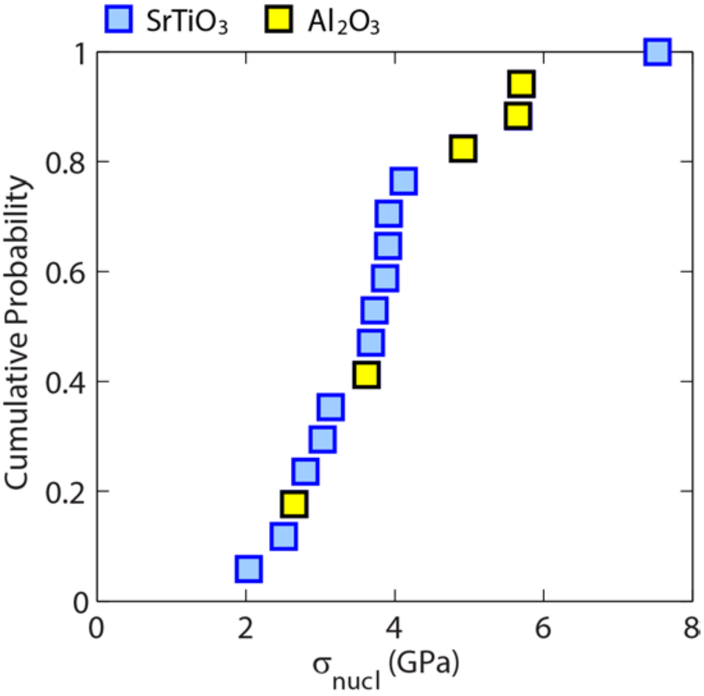

Figure S4. Experimental CDF distinguishing growth substrate for each specimen and the respective nucleation strength.

Table S2. Statistical parameters for two groups representing different growth substrates.

	$SrTiO_3$	**Al_2O_3**
Number of samples	12	5
Average σ_{nucl} (GPa)	3.69	4.51
Standard deviation (GPa)	1.44	1.34

The cumulative effect of these sources of experimental error is dominated by the uncertainty in the cross-section area. For most samples, this error is comparable to the uncertainties in diameter measurement and, consequently, in the resulting uncertainty in strength measurement displayed as error bars in Fig. 4(a) in main paper. Clearly the measured scatter at benchmark conditions alone surpasses the breadth of these uncertainties; therefore, we attribute the scatter primarily to the thermally activated nature of plastic deformation in these NWs.

Determining the Active Slip Systems in Pd NW Fracture Morphologies

In the case of the *in situ* TEM studies in the present work, the system and setup precluded us from recording diffraction patterns. However, we were able to obtain HRTEM images and compute their FFTs (see Fig. 2(g) and 2(i)), which provide equivalent information to diffraction and thus give the crystallography of our nanowhiskers. Beyond the orientations of the crystals, slip planes of the primary slip systems were determined to be $(1\bar{1}1)$ and $(\bar{1}11)$ based on the orientation of their trace lines relative to the FFT patterns, and slip planes of the secondary slip systems in Fig. 2(i) were assumed based on the known twinning transformation of $(\bar{1}11)$ with respect to $(1\bar{1}1)$. This analysis gave $(\bar{1}15)$ in the laboratory reference and agreed well with the orientation of trace lines in TEM image. Subsequently, the Burgers vectors of these slip systems were inferred to be those possessing the largest Schmid factors when loaded along NW axis $[1\bar{1}0]$, which are calculated as follows:

Table S3. Schmid factor analysis of possible primary slip systems. The activated systems are shown in red.

Full (Unit) Dislocations				*Partial Dislocations*					
$(1\bar{1}1)$ $[10\bar{1}]$	$(1\bar{1}1)$ $[0\bar{1}\bar{1}]$	$(\bar{1}11)$ $[101]$	$(\bar{1}11)$ $[0\bar{1}1]$	$(1\bar{1}1)$ $[1\bar{1}\bar{2}]$	$(1\bar{1}1)$ $[\bar{1}\bar{2}\bar{1}]$	$(1\bar{1}1)$ $[21\bar{1}]$	$(\bar{1}11)$ $[1\bar{1}2]$	$(\bar{1}11)$ $[\bar{1}\bar{2}1]$	$(\bar{1}11)$ $[211]$
0.408	0.408	0.408	0.408	0.471	0.236	0.236	0.471	0.236	0.236

Table S4. Schmid factor analysis of possible secondary slip systems, which are derived by twinning transformation of the corresponding primary systems in Table S3 with respect to $(1\bar{1}1)$. The activated system is shown in red.

Full (Unit) Dislocations				*Partial Dislocations*					
$(1\bar{1}1)$ $[10\bar{1}]$	$(1\bar{1}1)$ $[0\bar{1}\bar{1}]$	$(\bar{1}15)$ $[1\bar{4}1]$	$(\bar{1}15)$ $[4\bar{1}1]$	$(1\bar{1}1)$ $[1\bar{1}\bar{2}]$	$(1\bar{1}1)$ $[\bar{1}\bar{2}\bar{1}]$	$(1\bar{1}1)$ $[21\bar{1}]$	$(\bar{1}15)$ $[5\bar{5}2]$	$(\bar{1}15)$ $[721]$	$(\bar{1}15)$ $[\bar{2}\bar{7}1]$
0.408	0.408	0.227	0.227	0.471	0.236	0.236	0.262	0.131	0.131

It is interesting to notice that some slip systems (shown in green above) with larger Schmid factors were not observed in the twinning segment, and the only active secondary system $(\bar{1}15)[5\bar{5}2]$ can be considered as the transformation of the primary system $(\bar{1}11)[1\bar{1}2]$ across the twin plane $(1\bar{1}1)$. This indicates that plastic deformation of the NW shown in Fig. 2(i) was exclusively carried out by the dislocations that were activated upon yielding.

Development of and Results from the Analytical Model

Significance of the Stress Dependence α

The value of α represents the sensitivity of the activation energy to the applied stress: since the activation volume is $\Omega(\sigma,T) = -\partial\Delta G_{act}/\partial\sigma$, the decrease in the energy barrier due to mechanical work can drop dramatically near the athermal strength. Mechanistically, α is related to the particular obstacle that must be overcome during the thermally activated process. For example, for discrete obstacle-controlled plasticity in bulk crystals, $\alpha \approx 1$ (Ref. [6]). In addition, previous experimental studies extracting the activation parameters for dislocation nucleation assume a linear stress dependence of the activation free energy, i.e. $\Delta G_{act}(\sigma) = \Delta H_{act}(\sigma) = \Delta U_{act}(1 - \sigma/\sigma_{ath})$, where ΔH_{act} is the activation enthalpy. This results in a stress-independent activation volume $\Omega = \Delta H_{act}/\sigma_{ath}$, which is inconsistent with results found in many theoretical studies.

Aside from its mathematical simplicity and application in other experimental studies[7,8], it represents the weaker limit of stress dependence that has been identified in theoretical studies in literature[9]. A stronger stress dependence has been proposed ($\alpha \approx 4$) based on nudged elastic band (NEB) calculations of the activation energy for simulations of heterogeneous corner dislocation nucleation in a Cu NW under tension[1]. Therefore, the results of this latter case constitute the primary discussion in the main paper.

Significance of the Temperature Dependence T_m

Several simulation studies have identified a pronounced temperature dependence for ΔG_{act} attributed to effects arising from the stacking fault energy and anharmonicity[10,11]. The latter manifests as thermal expansion and thermal softening; given recent report of pronounced anharmonicity in Pd compared to other FCC metals[12], we hypothesize that entropic contributions to ΔG_{act} are non-negligible. While the analytical form for the temperature dependence in Eq. 2 has been a matter of some debate[10,11,13], it enables an estimate of the maximum activation entropy, $-\partial\Delta G_{act}/\partial T|_{\sigma=0} = \Delta U_{act}/T_m$. For $\alpha = 4$, we take T_m to be the surface-disordering temperature[1] since the bonding at the surface can significantly affect the thermal and mechanical properties contributing to the activation entropy[14]. The value of T_m can vary significantly for different surfaces orientations[15], however, the results of the model for nucleation strength are insensitive to the choice of T_m for our testing conditions (Fig. S5). For simplicity, we use the convention of approximating T_m as half the bulk melting temperature. In the case of $\alpha = 1$, it should also be noted that ΔG_{act} in these earlier studies has been treated as temperature-independent, and we maintain this convention for this case only.

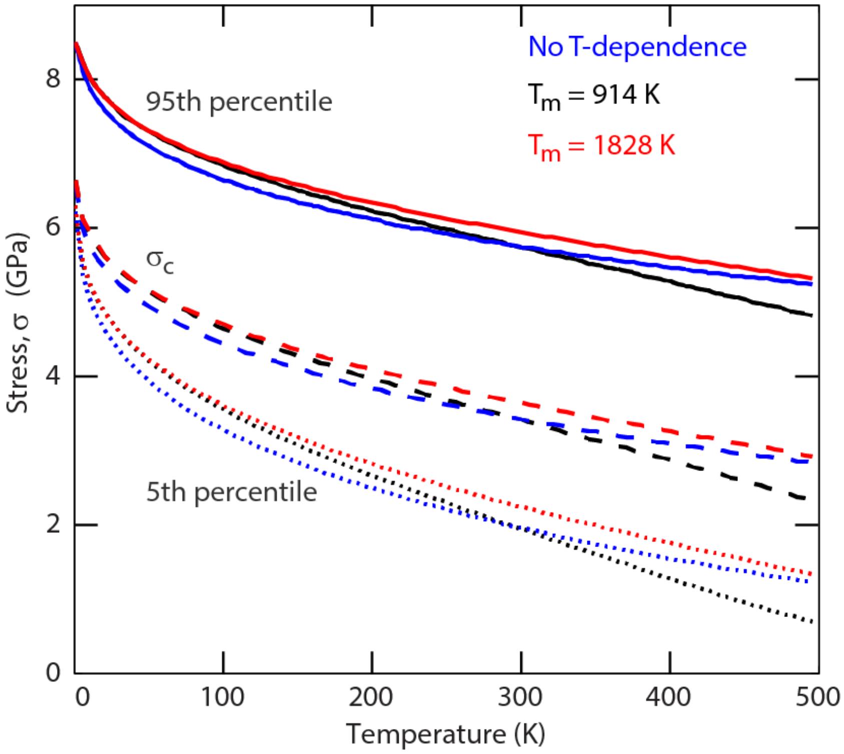

Figure S5. Sensitivity of analytical model to choice of critical temperature. Predicted critical stress (σ_c) and percentile lines are based on the activation energy formula presented in Eq. 2 and solved for $\alpha = 4$. The case of $T_m = 914$ K (black lines) is assumed for the main analysis, and the calculated percentile lines correspond to those in Figure 6(b). The case of "No T-dependence" (blue lines) is calculated by removing the temperature-dependence term $\left(1-\frac{T}{T_M}\right)$ from Eq. 2. The largest differences between $T_m = 914$ K and the other temperature cases arises at and above the higher end of the current experimental temperature range.

Determining the Thermal Activation Parameters for Weak Stress Dependence of the Activation Energy (α = 1)

For a given strain rate and temperature, the spread of measured yield strengths provides a cumulative distribution function, to which an assumed analytical model can be applied. From transition state theory (TST), the rate of dislocation nucleation v can be expressed as:

$$\nu = \begin{cases} N\nu_0 \exp\left(-\frac{\Delta U_{act}}{k_B T}\right)\exp\left(\frac{E\dot{\varepsilon}t\Omega}{k_B T}\right) \text{ for } 0 \le \sigma \le \sigma_{\text{ath}} \\ N\nu_0 \text{ for } \sigma > \sigma_{\text{ath}} \end{cases} \qquad \text{Eq. S1}$$

where we assume $\sigma = E\dot{\varepsilon}t$, where E is the small-strain Young's modulus and $\dot{\varepsilon}$ is the strain rate (average of $3.88\text{x}10^{-4}$ s^{-1} for benchmark experiments). This formulation takes into account that even in the absence of an energy barrier, nucleation is limited by the kinetics of the system. Plugging this into the following expression for the cumulative distribution function (CDF)[16,17]

$$F(t) = 1 - \exp\left(-\int \nu(t)dt\right) \qquad \text{Eq. S2a}$$

yields the following expression valid up to σ_{ath}:

$$F(\sigma,T) = 1 - \exp\left(\frac{N\nu_0 k_B T}{E\dot{\varepsilon}\Omega}\left[\exp\left(-\frac{\Delta U_{act}}{k_B T}\right) - \exp\left(\frac{\Omega\sigma - \Delta U_{act}}{k_B T}\right)\right]\right) \text{ for } 0 \le \sigma \le \sigma_{ath} \qquad \text{Eq. S2b}$$

Fitting Eq. S2b to the experimental CDF yields solutions for the relevant parameters Ω, $N\nu_0$, and ΔU_{act}. For Ω, we obtain a value of 4.79 Å^3 or $0.23b^3$, where b is the full Burger's vector in Pd. Similar to the $\alpha = 4$ case, this fitted value for Ω is lower than the range of 1-$10b^3$, which has been theoretically predicted for heterogeneous nucleation[1]. For the fitting of the rate prefactor $N\nu_0$ to the experimental we obtain 0.47 s^{-1}, orders of magnitude lower than theoretical predictions based on the Debye frequency (as discussed in the main text). However, this prefactor is also consistent with the expectation time provided in the load-hold test in the main paper, yielding an expectation time of 150 s at 3.8 GPa.

From Eq. S2*b* it is also possible to extract values for ΔU_{act} from the room temperature CDF. While the value for ΔU_{act} (and thereby the athermal strength) should be determined by temperature-dependent behavior, this fit provides an initial estimate of 0.18 eV. To comprehensively evaluate the temperature-dependent behavior and extract ΔU_{act}, Eq. S2b is solved for stress as a function of temperature:

$$\sigma(T)=\frac{k_BT}{\Omega}\ln\left(\exp\left(-\frac{\Delta U_{act}}{k_BT}\right)-\frac{E\dot{\varepsilon}\Omega}{k_BTN\nu_0}\ln\left(1-F(\sigma)\right)\right)+\frac{\Delta U_{act}}{\Omega}\ \text{for } 0\le\sigma\le\sigma_{\mathrm{ath}} \qquad \text{Eq. S3}$$

This yields ΔU_{act} = 0.23 eV, which agrees well with the fit derived from the room-temperature CDF alone of 0.18 eV. At room temperature, σ_c is then 5.85 GPa, leading to a $\Delta H_{act} = \Delta U_{act} - \Omega\sigma$ of 0.047 eV, which is still lower than predictions from NEB calculations for partial dislocation nucleation in single-crystal Cu NWs (0.1 and 0.6 eV)[1]. Nonetheless, the current value for ΔU_{act} yields an athermal strength σ_{ath} in Pd NWs of 7.46 GPa, which is comparable to the highest strengths measured at low temperatures. The values for σ_{ath} for α = 1 and α = 4, resolved along the primary slip system and with respect to the shear modulus μ = 44 GPa, are 0.080μ and 0.076μ, respectively. These values for heterogeneous nucleation closely approach reported values from ab initio calculations of the theoretical shear strength in Pd of 0.084μ[18] and 0.087μ[19].

Derivation of F(σ) for α = 4

Using the expression for ΔG_{act} in Eq. 2 in the main text with $\alpha = 4$ and $\sigma = E\dot{\varepsilon}t$, $F(\sigma)$ becomes:

$$\begin{aligned}F(\sigma,T)&=1-\exp\left[-\frac{1}{E\dot{\varepsilon}}\int_0^{\sigma}\nu(\sigma')d\sigma'\right] \qquad \text{Eq. S4}\\&=1-\exp\Bigg\{\frac{N\nu_0}{E\dot{\varepsilon}}\Bigg[\frac{\sigma_{ath}}{4}\left(\frac{\Delta U_{act}}{k_B}\left(\frac{1}{T}-\frac{1}{T_M}\right)\right)^{-1/4}\Bigg(\Gamma\left[\frac{1}{4},\frac{\Delta U_{act}}{k_B}\left(\frac{1}{T}-\frac{1}{T_M}\right)\right]-\Gamma\left[\frac{1}{4},\frac{\Delta U_{act}}{k_B}\left(\frac{1}{T}-\frac{1}{T_M}\right)\left(1-\frac{\sigma}{\sigma_{ath}}\right)^4\right]\Bigg]\Bigg)\end{aligned}$$

In the above expression, $\Gamma(a,x)=\int_x^{\infty}t^{a-1}e^{-t}dt$ is the upper gamma function. Note that the above expression is only valid for $0\le\sigma\le\sigma_{ath}$; a second expression for $f(\sigma,T)$ above σ_{ath} accounts for nucleation kinetically limited by the maximum rate even in the absence of an energy barrier, i.e. $\nu(\sigma) = N\nu_0$ for $\sigma > \sigma_{ath}$.

Analytical Solution above the Athermal Strength for Kinetically-limited Dislocation Nucleation

Above the athermal strength, there is no finite energy barrier and the maximum rate of nucleation events is $\nu_{max} = N\nu_0$ for $\sigma > \sigma_{ath}$. Assuming an attempt frequency ν_0 on the order of the Debye frequency leads to "instantaneous" nucleation with an expectation time <10^{-13} s. However, for the very low ν_{max} obtained from the current experiments of ~10^{-1} s^{-1} and applied strain rates only a few orders of magnitude lower, there is finite probability that nucleation occurs above σ_{ath}.

To solve for the cumulative distribution above σ_{ath} and account for ν_{max}, Eq. S2a must be solved up to an arbitrary value of $\sigma > \sigma_{ath}$. For $\alpha = 1$, this leads to:

$$F(\sigma,T) = 1 - \exp\left(-\int_0^{\sigma_{ath}} \frac{N\nu_0}{E\dot{\varepsilon}} \exp\left(-\frac{\Delta U_{act} - \Omega\sigma'}{k_B T} \right) d\sigma' - \int_{\sigma_{ath}}^{\sigma} \frac{N\nu_0}{E\dot{\varepsilon}} d\sigma' \right)$$

$$= 1 - \exp\left(\frac{N\nu_0 k_B T}{E\dot{\varepsilon}\Omega} \left[\exp\left(-\frac{\Delta U_{act}}{k_B T} \right) - 1 - \frac{\Omega\sigma - \Delta U_{act}}{k_B T} \right] \right) \text{ for } \sigma > \sigma_{ath} \qquad \text{Eq. S5}$$

The derivative of $F(\sigma,T)$ with respect to σ then yields the PDF solution used to plot Fig. 6(a) above σ_{ath} in the main text. The continuation of the 95th percentile contour line above σ_{ath} is then:

$$\sigma(T) = \frac{k_B T}{\Omega}\left(\exp\left(-\frac{\Delta U_{act}}{k_B T} \right) - 1 \right) - \frac{E\dot{\varepsilon}}{N\nu_0}\log(1 - F(\sigma)) + \frac{\Delta U_{act}}{\Omega} \text{ for } \sigma > \sigma_{\text{ath}} \qquad \text{Eq. S6}$$

The same approach shown in Eq. S4 is used for $\alpha = 4$ to solve for $F(\sigma,T)$, leading to:

$$F(\sigma,T) = 1 - \exp\left(\frac{N\nu_0}{E\dot{\varepsilon}} \left[\frac{\sigma_{ath}}{4} \left(\frac{\Delta U_{act}}{k_B} \left(\frac{1}{T} - \frac{1}{T_M} \right) \right)^{-1/4} \left(\Gamma\left[\frac{1}{4}, \frac{\Delta U_{act}}{k_B} \left(\frac{1}{T} - \frac{1}{T_M} \right) \right] - \Gamma\left[\frac{1}{4} \right] \right) + \sigma_{ath} - \sigma \right] \right) \text{ for } \sigma > \sigma_{ath} \qquad \text{Eq. S7}$$

Discussion of Nucleation Rate Prefactor

The computed nucleation rate prefactor $N\nu_0$ of 0.065 s^{-1} ($\alpha = 4$) can be compared to time scales for nucleation measured in our experiments. The load-hold test performed and shown in Fig. 1(b) represents a case where a fixed load is applied below the fracture strength and nucleation is assisted by thermal fluctuations and time. These experiments suggest a nucleation expectation time of 24 s at 3.8 GPa, which agrees with our model's prediction of the order of 10 s. Similar to other experimental studies[7,16], our computed nucleation rate prefactors are approximately nineteen orders of magnitude different from a value that can be estimated assuming the truncated rhombic cross-sectional geometry of the NW and an attempt frequency on the order of the Debye frequency (5.7×10^{12} s^{-1}). This implies that even a single viable activation site on the surface of our Pd NW ($N = 1$) would possess an attempt frequency of the order of 0.01 s^{-1}. While there have been studies demonstrating a different vibrational frequency of surface atoms from the bulk[20], these manifest primarily in small changes of the surface Debye temperature, which alone cannot account for such a large discrepancy. Given that dislocation nucleation does not involve single atoms but rather a collective group, the frequency of individual atomic vibrations may not be a suitable or physically sensible attempt frequency[21].

Based on the fittings of the experimental data to our models for both weak and strong stress dependence of the activation energy, we obtain the nucleation parameters summarized in Table S5.

Table S5. Thermal activation parameters for different stress dependences of the activation energy. Athermal strength σ_{ath} is reported in terms of both absolute value and fraction of the shear modulus μ.

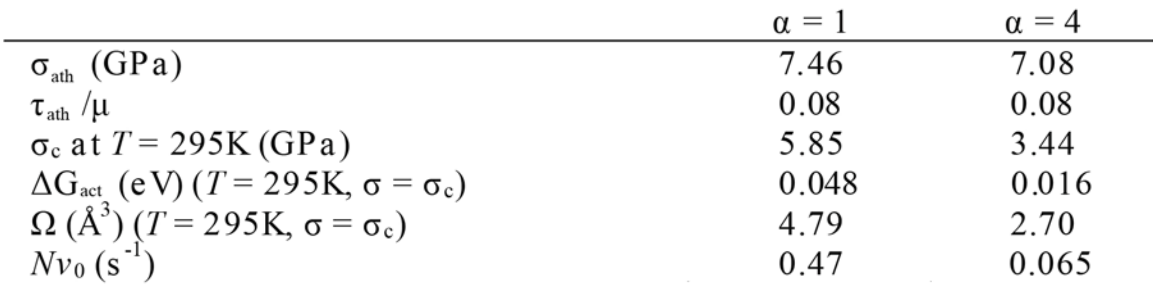

	$\alpha = 1$	$\alpha = 4$
σ_{ath} (GPa)	7.46	7.08
τ_{ath}/μ	0.08	0.08
σ_c at $T = 295$K (GPa)	5.85	3.44
ΔG_{act} (eV) ($T = 295$K, $\sigma = \sigma_c$)	0.048	0.016
Ω (Å^3) ($T = 295$K, $\sigma = \sigma_c$)	4.79	2.70
$N\nu_0$ (s^{-1})	0.47	0.065

We note that the activation parameters deduced from our study and calculated for both values of α, most notably the kinetic prefactor $N\nu_0$, are still below the values obtained in computational studies. The experimental values of $N\nu_0$ remain only a few orders of magnitude higher than the applied strain rate, so even in the absence of a finite energy barrier (e.g. $T < 100$ K, $\sigma > \sigma_{ath}$) nucleation is kinetically limited by the attempt frequency and thus not necessarily instantaneous. This leads to non-zero probabilities for nucleation above σ_{ath}, as observed in the analytical results plotted in Fig. 6.

Comparison of Two Cases of α

Statistically speaking, our experiments demonstrate better agreement with $\alpha = 4$, with about 90% of the measured events falling within the contoured envelope (Fig. 6(b)). However, the agreement between the calculated temperature dependence of σ_c and the experimental results at low temperature suggest that an α closer to unity represents the physical obstacles to dislocation nucleation more accurately. This is also seen in Fig. S6, where a rough comparison is provided through averaging the measured strengths within a given temperature window. While the magnitude of the difference between each case and the experimental averages is similar, the agreement varies with temperature: at lower temperatures $\alpha = 1$ agrees better with the temperature whereas $\alpha = 4$ better models the higher temperature behavior.

As mentioned in the main text, it is within this low temperature regime approaching 0 K where the two models are most distinguishable and therefore where experiments can best inform the stress dependence of the activation energy. A similar observation has been noted in simulations of FCC crystals of varying geometries, which effectively change the "shape" of the obstacle that must be overcome[22].

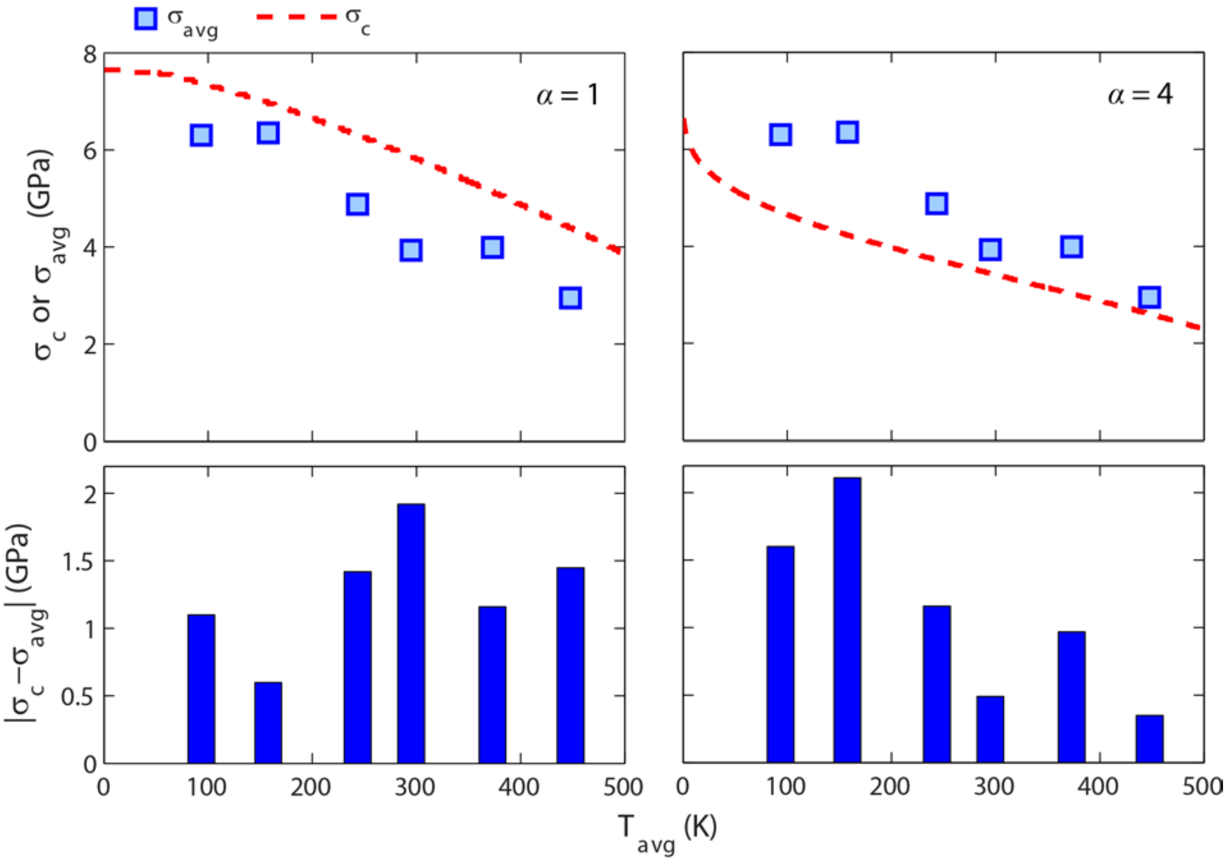

Figure S6. Comparison between experimental mean strength σ_{avg} and calculated most probable strength σ_c. T_{avg} represents the average temperature for each temperature window over which σ_{avg} was calculated. The lower bar graphs show the difference between experiment and model at each T_{avg}.

References

1. Zhu, T., Li, J., Samanta, A., Leach, A. & Gall, K. Temperature and Strain-Rate Dependence of Surface Dislocation Nucleation. *Phys. Rev. Lett.* **100,** 025502 (2008).

2. Murphy, K. F., Chen, L. Y. & Gianola, D. S. Effect of organometallic clamp properties on the apparent diversity of tensile response of nanowires. *Nanotechnology* **24,** 235704 (2013).

3. Hillier, J. On the Investigation of Specimen Contamination in the Electron Microscope. *J. Appl. Phys.* **19,** 226 (1948).

4. Ennos, A. E. The origin of specimen contamination in the electron microscope. *Br. J. Appl. Phys.* **4,** 101–106 (1953).

5. Ding, W. *et al.* Mechanics of hydrogenated amorphous carbon deposits from electron-beam-induced deposition of a paraffin precursor. *J. Appl. Phys.* **98,** 014905 (2005).

6. Frost, H. J. & Ashby, M. F. *Deformation-Mechanism Maps*. (Pergamon Press Inc., 1982).

7. Wo, P. C., Zuo, L. & Ngan, a. H. W. Time-dependent incipient plasticity in Ni3Al as observed in nanoindentation. *J. Mater. Res.* **20,** 489–495 (2011).

8. Schuh, C. a, Mason, J. K. & Lund, a C. Quantitative insight into dislocation nucleation from high-temperature nanoindentation experiments. *Nat. Mater.* **4,** 617–21 (2005).

9. Wang, L. *et al.* Determining the activation energies and slip systems for dislocation nucleation in body-centered cubic Mo and face-centered cubic Ni single crystals. *Scr. Mater.* **65,** 179–182 (2011).

10. Warner, D. H. & Curtin, W. a. Origins and implications of temperature-dependent activation energy barriers for dislocation nucleation in face-centered cubic metals. *Acta Mater.* **57,** 4267–4277 (2009).

11. Ryu, S., Kang, K. & Cai, W. Entropic effect on the rate of dislocation nucleation. *Proc. Natl. Acad. Sci. U. S. A.* **108,** 5174–8 (2011).

12. Chen, L., Richter, G., Sullivan, J. & Gianola, D. Lattice Anharmonicity in Defect-Free Pd Nanowhiskers. *Phys. Rev. Lett.* **109,** 125503 (2012).

13. Ryu, S., Kang, K. & Cai, W. Predicting the dislocation nucleation rate as a function of temperature and stress. *J. Mater. Res.* **26,** 2335–2354 (2011).

14. Gu, M. *et al.* Size, temperature, and bond nature dependence of elasticity and its derivatives on extensibility, Debye temperature, and heat capacity of nanostructures. *Phys. Rev. B* **75,** 125403 (2007).

15. Kern, K. in *Phase Transitions Adsorbate Restruct. Met. Surfaces, Chem. Phys. Solid Surfaces* 291–340 (Elsevier, 1994).

16. Mason, J., Lund, a. & Schuh, C. Determining the activation energy and volume for the onset of plasticity during nanoindentation. *Phys. Rev. B* **73,** 054102 (2006).

17. Zuo, L. & Ngan, a. H. W. Molecular dynamics study on compressive yield strength in Ni3Al micro-pillars. *Philos. Mag. Lett.* **86,** 355–365 (2006).

18. Hartford, J., von Sydow, B., Wahnström, G. & Lundqvist, B. Peierls barriers and stresses for edge dislocations in Pd and Al calculated from first principles. *Phys. Rev. B* **58,** 2487–2496 (1998).

19. Kamran, S., Chen, K. & Chen, L. Ab initio examination of ductility features of fcc metals. *Phys. Rev. B* **79,** 024106 (2009).

20. Rabkin, E. & Srolovitz, D. J. Onset of plasticity in gold nanopillar compression. *Nano Lett.* **7,** 101–7 (2007).

21. Kocks, U. F., Argon, A. . & Ashby, M. F. *Thermodynamics and Kinetics of Slip*. (Argonne National Laboratory, 1973).

22. Brochard, S., Hirel, P., Pizzagalli, L. & Godet, J. Elastic limit for surface step dislocation nucleation in face-centered cubic metals: Temperature and step height dependence. *Acta Mater.* **58,** 4182–4190 (2010).